Computational Modelling of Gas-Particle Flows with Different Particle Morphology in the Human Nasal Cavity

Kiao Inthavong[1], Jiyuan Tu[1], Goodarz Ahmadi[2]
[1]School of Aerospace, Mechanical and Manufacturing Engineering, RMIT University, Victoria, Australia
[2]Department of Mechanical and Aeronautical Engineering, Clarkson University, Potsdam, New York, USA

Abstract
This paper summarises current studies related to numerical gas-particle flows in the human nasal cavity. Of interest are the numerical modelling requirements to consider the effects of particle morphology for a variety of particle shapes and sizes such as very small particles sizes (nanoparticles), elongated shapes (asbestos fibres), rough shapes (pollen), and porous light density particles (drug particles) are considered. It was shown that important physical phenomena needed to be addressed for different particle characteristics. This included the Brownian diffusion for submicron particles. Computational results for the nasal capture efficiency for nano-particles and various breathing rates in the laminar regime were found to correlate well with the ratio of particle diffusivity to the breathing rate. For micron particles, particle inertia is the most significant property and the need to use sufficient drag laws is important. Drag correlations for fibrous and rough surfaced particles were investigated to enable particle tracking. Based on the simulated results, semi-empirical correlations for particle deposition were fitted in terms of Peclet number and inertial parameter for nanoparticles and micron particles respectively.

Keywords: Nasal cavity; Fibres; Pollen; Nanoparticle; Deposition; CFD

INTRODUCTION

Modelling gas-particle flows in the nasal cavity poses many challenges. Firstly the nasal cavity is highly complex characterised by narrow airway channels with many curves and indentations from the surrounding facial bones. Detailed air flow patterns can provide data that is pertinent to the prediction of gas-particle flows. However the small dimensions prevent direct measurements of flow patterns inside the human nose. Two alternatives have been readily adopted. The first being experimental methods, performed by many researchers (Girardin et al. 1983; Hahn et al. 1993; Hornung et al. 1987; Schreck et al. 1993; Swift and Proctor 1977) whereby rigid cast models have been used to study the airflow patterns. More recent experimental work also include that of Park et al. (1997a), Park et al. (1997b), and Kelly et al. (2000). Because of the lack of fine details associated with cast models, the other alternative is numerical simulations which have been performed to complement the existing experimental data. Of note is the early works of Elad et al. (1993) and Keyhani et al. (1995; Keyhani et al. (1997). Subramaniam et al. (1998) simulated the airflow under steady-state, inspiratory conditions simulating rest and light exercise (steady-state inspiratory flow rates). Hörschler et al. (2003) simulated a realistic model of the nasal cavity using a computational code developed at the Aerodynamisches Institut, *RWTH Aachen*, Germany. Other studies include Weinhold and Mlynski (2004), Zhao et al. (2004), Wang et al. (2005) Naftali et al. (2005), Lindemann et al. (2006), and Croce et al. (2006) which simulated the airflow at rest and light breathing conditions (between 10L/min and 26L/min) using a laminar flow regime. These studies focussed on one side of the nasal cavity and comparisons of the flow patterns between both nostrils were not made. A comparative study of airflow patterns between different models was performed by Wen et al. (2008).

Gas-particle flow analysis has focussed on the fate of individual particles dispersed in a dilute phase and hence allows one-way coupling between the particle and the gas phase. This obviates the difficulties associated with fully coupling the gas-particle interactions, such as turbulence modulation. Experimental methods have been performed which has helped to validate the numerical simulations. *In vitro* studies involve all physiological parameters using human volunteers, however is highly invasive due to the use of probes or radio-labelled particles which usually require large amounts of radioactivity. To avoid these problems and to obtain more reproducible results, *in vitro* studies using replicate casts have also been carried out (Cheng et al. 1998; Gradon and Podgorski 1992; Guilmette et al. 1994; Häußermann et al. 2001; Itoh et al. 1985; Kelly et al. 2004; Swift 1991; Zwartz and Guilmette 2001).

Numerical simulations for gas-particle flows in the human nasal cavity have studied a range of particles. The simulation of nanoparticle deposition was performed by Zamankhan et al. (2006) under steady laminar conditions where diffusion was the dominant deposition mechanism for the smallest range of particles (1–30 nm). Shi et al. (2006) and Shi et al. (2008) also simulated the transport and deposition of nanoparticles, d_p=1-2 nm and ultrafine particles, d_p=5 nm under a transient laminar flow in a representative human nasal cavity. In a follow up study by the same authors (Shi et al. 2007) inertial particles in the human nasal cavity were simulated, where the wall roughness of the nasal cavity was taken into account. Schroeter et al. (2006) employed CFD to analyse particle deposition in the nasal cavity particularly in the turbinate and olfactory region which is important in the understanding of the olfaction and its physiology. Other particle deposition simulations include Tian et al. (2007) who investigated spherical wood dust particles and Tu et al. (2004) who investigated particles with different densities.

In the pharmaceutical industry where nasal sprays have become a realistic alternative to traditional routes of drug delivery, simulations of sprayed particles within the nasal cavity have been performed. Kimbell et al. (2004) simulated particle deposition by releasing particles from different planes in order to imitate the nasal spray delivery. In a follow-up paper by the same research group (Kimbell et al. 2007), particles were released from different locations of the nostrils to characterise the deposition efficiencies and patterns from nasal sprays. Djupesland et al. (2003) also demonstrated the use of CFD to design a novel nasal spray device that prevented deep lung deposition of drug particles. A study by the authors tested different parameters associated with the design of nasal sprays and its effect on the deposition patterns of the particles (Inthavong et al. 2006).

Another challenging problem with gas-particle flows in the nasal cavity is the application of turbulence models. In the above mentioned studies related to sprayed particles one way coupling was used although in the atomisation of a spray, the local void fraction may actually exceed the dilute phase assumption inherent in one way coupling. Turbulence modelling is already difficult in single phase, while in multiphase the complexity increases even further. Two-equation Reynolds Averaged Navier-Stokes (RANS) turbulence models are designed for flows that are fully turbulent, although modifications have been made to formulate low-Reynolds number models that reproduce the transitional behaviour from laminar to turbulent flow. However in these models the physics of transitional flow behaviour is not actually resolved and in low flow rates, where laminar effects are dominant, turbulence models provide greater diffusion due to the turbulent viscosity term:

$$\mu_{eff} = \mu_m + \mu_t \tag{1}$$

where μ_{eff} is the effective viscosity, μ_m is the molecular viscosity, and μ_t is the turbulent viscosity. Sophisticated models such as Large Eddy Simulations (LES) and Direct Numerical Simulations can resolve the transitional behaviour but are quite computationally expensive.

In one-way coupled turbulent dispersion of particles, the isotropic turbulence assumption of RANS turbulence models becomes problematic in wall bounded flows such as the nasal cavity. The turbulent dispersion of particles is determined by the stochastic process through the so-called 'Discrete Random Walk' model (DRW). This method is also referred to as the Eddy Interaction Model (EIM). Within this model the fluctuating velocity components u_i' are taken from the local root mean square (RMS) velocity fluctuation by

$$\sqrt{\overline{u_i'^2}} = \sqrt{2k_g / 3} \tag{2}$$

However the isotropic assumption (i.e. $u' = v' = w'$) leads to an overestimation of the normal fluctuating velocity component in the near wall region. This causes an overestimation of deposition for the smaller range of particles (<10μm) (Macinnes and Bracco 1992; Wang and James 1999; Zhang et al. 2004). This overestimation at the near wall region increases in sensitivity for smaller particles that have a shorter relaxation time. Improved models for the DRW model is proposed by Wang and James (1999), Matida et al. (2004), and Dehbi (2008), Tian and Ahmadi (2007). These models effectively 'damp' out the normal fluctuating velocity or makes use of an alternative stochastic process. These subroutines require accessing and modifying the variables within the commercial CFD codes the simulations are run on, which is quite difficult. A simpler alternative was proposed by the authors in Inthavong et al. (2006) to use mean flow tracking for the smaller range particles (<10μm) while for larger particles turbulent tracking was sufficient. To obviate the need to rectify the isotropic assumption problem, the use of anisotropic turbulent models can be applied. A possibility is to use Large Eddy Simulations (LES) which is quite computationally expensive and requires a robust boundary conditions and high quality mesh set up. The only study involving LES so far has been performed by Liu et al. (2007) which compared the turbulent particle dispersion under different turbulent models. More recently the v2-f model has been found to model the near wall anisotropy well, however its application to the nasal cavity flow has yet to be reported.

Another challenge of modelling gas-particle flows is taking into consideration the particle morphology. It is apparent that different particles such as fibres, pollen and porous particles will exhibit significantly different shapes and densities which undermine the aerodynamic properties of the aerosol. Crowder et al. (2002) points out the importance of particle morphology in the deposition of particles in the lungs, citing the importance of particle density, shape, size and surface characteristics (roughness, electrical charge, vapour pressure etc.). Numerical simulations of gas-particle flows in the nasal cavity have mainly focussed on spherical particles and turbulence models while lacking in the investigation of different particle morphology. Unfortunately experimental investigations of particle deposition are also limited to spherical particles (Kelly et al. 2004; Häuβerman et al. 2001; Zwartz and Guilmette 2001) where deposition efficiencies have been correlated with an impaction parameter. More recently there has been research dealing with fibre deposition (Su and Cheng 2005). This paper discusses some techniques required to model gas-particle flows in the human nasal cavity. Of interest will be the setup of the flow boundary conditions and numerical considerations for different particle morphology. Specifically particle characteristics such as: very small particles sizes (nanoparticles), elongated shapes (asbestos fibres), rough shapes (pollen), and porous light density particles (drug particles) are considered.

AIRWAY GEOMETRY AND NUMERICAL MODELS

CT scans and Image Segmentation

The nasal cavity geometry was obtained through a CT scan of a healthy 25 year old, Asian male (170 cm height, 75 kg mass). The CT scan was performed using a CTI Whole Body Scanner (General Electric). The single-matrix scanner was used in helical mode with 1-mm collimation, a 40-cm field of view, 120 kV peak and 200 mA. The scans captured outlined slices in the *X*-*Y* plane at different positions along the *Z*-axis from the entrance of the nasal cavity to just anterior of the larynx at intervals of 1 to 5 mm depending on the complexity of the anatomy. The coronal sectioned scans were imported into a three-dimensional (3D) modelling program called GAMBIT (ANSYS Inc., USA) which created smooth curves that connected points on the coronal sections. Stitched surfaces were then created to form a complete computational mesh. Because the details of the flow velocity and pressure were not known prior to the solution of the flow problem, the outlet boundary condition was defined as an outflow with zero diffusion flux for all flow variables in the direction normal to the exit plane. This implies that the flow characteristics have to be consistent with a fully-developed flow assumption and a straight extension of the outlet plane was created into the geometry to satisfy this criterion.

An initial model with 82,000 unstructured tetrahedral cells was initially used to solve the air

flow field at a flow rate of 15L/min. The model was then improved by cell adaptation techniques that included refining large volume cells, cells that displayed high velocity gradients and near wall refinements, where a model with a higher cell count was produced. This process was repeated twice, with each repeat producing a model with a higher cell count than the previous model. Subsequently four models were produced, 82000, 586000, 950000 and 1.44million cells. A grid independence test found the results for average velocity and the wall shear stress converge as the mesh resolution approached 950,000 cells. In order to make a compromise between the result's accuracy and computational cost, a model with 950,000 elements was used in this study (Figure 1).

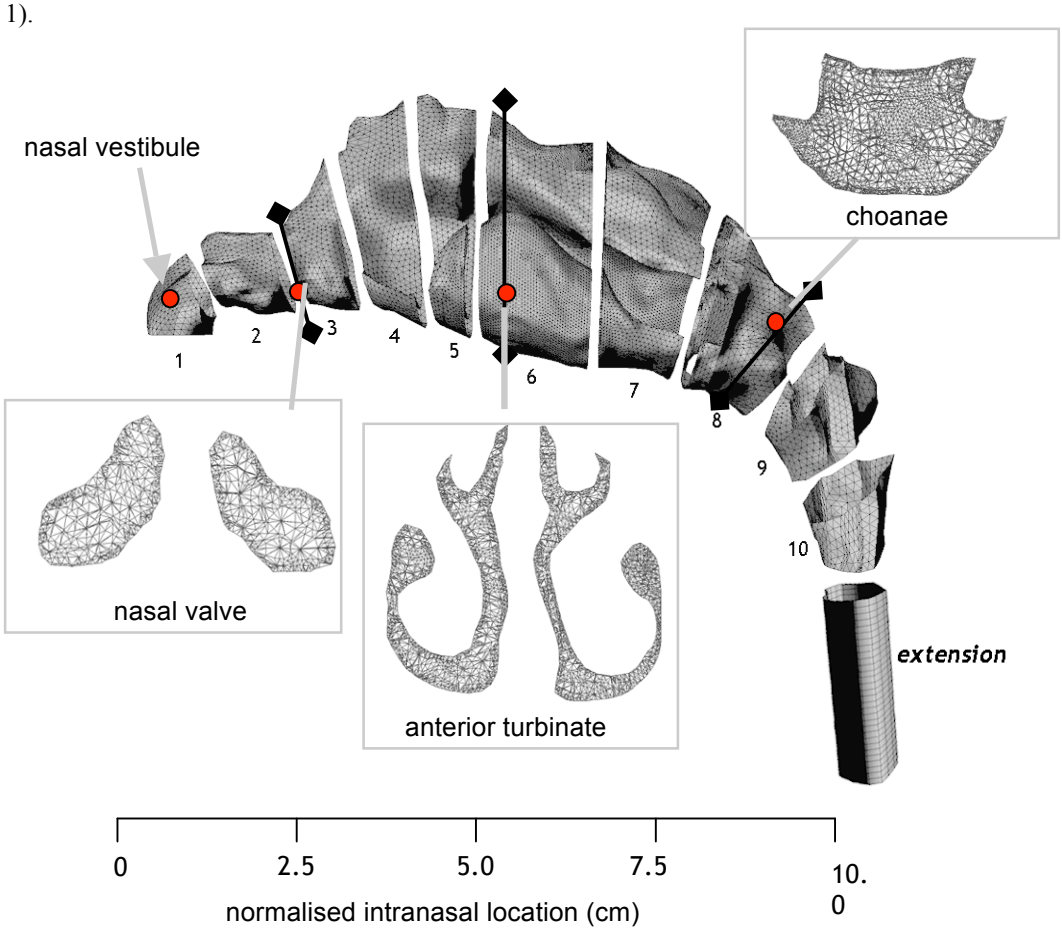

Figure 1. Nasal cavity model used in the study. Cross-sectional areas taken at the nasal valve, middle turbinate and nasopharaynx regions are shown with the computational mesh.

FLUID FLOW MODELLING

Due to the complex geometry of the nasal cavity a commercial CFD code, FLUENT, was utilised to predict the continuum gas phase flow under steady-state conditions through solutions of the conservation equations of mass and momentum. These equations were discretised using the finite volume approach. The third order accurate QUICK scheme was used to approximate the momentum equation whilst the pressure-velocity coupling was resolved through the SIMPLE method. Flow rates ranging from 7.5L/min to 15L/min were used to simulate light adult breathing. Flow rates up to 15L/min have been determined to be laminar (Hahn et al. 1993; Swift and Proctor 1977). A steady flow rather than a cyclic unsteady flow was used in this case to allow the results to emphasize the airflow dynamics and patterns independent from cyclic conditions. Moreover the significance of the fluctuating sinusoidal pattern of the inhalation-exhalation breathing cycle on the nasal airflow can be estimated by examining the Womersley number, α and the Strouhal number, *S*. The calculated Womersley number,

$$\alpha = \frac{D}{2}\left(\frac{\omega}{\nu_g}\right)^{0.5} \tag{3}$$

was 1.68 while the Strouhal number,

$$S = \frac{\omega D}{u_{ave}} \tag{4}$$

was 0.01. D is equal to 0.01m and is the characteristic length which was taken as the average hydraulic diameter of thirty cross-sections taken throughout the nasal cavity. ν_g is the kinematic viscosity of air and ω is the breathing frequency equal to $\omega = 2\pi f = 1.57 s^{-1}$ and u_{ave} is the average velocity through the nasal passage under the flow rate of 15L/min which is equal to 0.9m/s. Although the Womersley number is greater than 1, it is not much greater, while the low value for S suggests that the flow may be assumed to be quasi-steady. It has however, been shown experimentally that the oscillatory effects are not present until α => 4 (Isabey and Chang (1981). Additionally other studies have also concluded that under most conditions especially low flow rates, the nasal airflow can be considered quasi-steady (Chang 1989; Hahn et al. 1993; Sullivan and Chang 1991).

The steady-state continuity and momentum equations for the gas phase (air) in Cartesian tensor notation are:

$$\frac{\partial}{\partial x_i}\left(\rho_g u_i^g\right) = 0 \tag{5}$$

$$\rho u_j^g \frac{\partial u_i^g}{\partial x_j} = -\frac{\partial p_g}{\partial x_i} + \frac{\partial}{\partial x_j}\left(\mu_g \frac{\partial u_i^g}{\partial x_j}\right) \tag{6}$$

where u_i^g is the i-th component of the time averaged velocity vector and ρ_g is the air density.

AIRFLOW BOUNDARY CONDITIONS

For the boundary conditions, a no slip flow velocity on the passage surfaces was assumed. At the nostril, a uniform flow perpendicular to the inlet was specified which is a reasonable approximation. Keyhani et al. (1995) specified the velocity profile at the nostril based on experimental data which showed that for a given flow rate the downstream flow field is not significantly affected by the details of the velocity profile at the nostril. Additionally the flow rates of left and right nostrils are assumed to be the same. This does not simulate real breathing perfectly since the flow is induced at the larynx drawing the air from the nostrils which is affected by geometrical differences leading to varied flow rates between the cavities. However for comparative purposes, each nostril should have the same flow rate passing through to allow the effects of the geometry and particle morphology to be investigated.

FACTORS INFLUENCING DEPOSITION MECHANISMS IN THE NASAL CAVITY

Individual aspects of the nasal cavity such as the geometry and flow rate collectively affect the airflow patterns and consequently the transport of particles through the cavity. Significant anatomical factors include the nasal length, the bend from the nostrils into the cavity (Inthavong et al. 2006) and structure of the turbinates (Churchill et al. 2004). Deposition of particles in the nasal cavity is usually in the form of four mechanisms: inertial impaction and Brownian diffusion, and to a lesser extent, gravitational sedimentation and interception (Figure 2). Deposition by interception may be more present for fibres due to its elongated shape. Deposition by interception can occur if the particle travels close enough to a surface of the airway passages where an edge of the particle touches the surface. Deposition by interception is usually low due to the differences in dimensional magnitudes – fibre length ≈ 10^{-6} compared with airway geometry ≈ $10^{-3.}$ Gravitational sedimentation is also less dominant as it requires that the particle is settling in the airway due to an

absence of convective flow in the gas phase. Deposition of submicron particles will mainly deposit by Brownian diffusion. In the submicron range, as the particle size approaches 1nm the effects of Brownian diffusion becomes increasingly dominant. For micron ranged particles, typically larger than 1μm, the effects of particle inertia become important and deposition by inertial impaction becomes dominant. Inertial impaction occurs due to the particles not being able to follow the air streamlines, instead continuing more tangentially and depositing on the near wall. The inertial impaction parameter is used to define the particles impactability and is given as,

$$I = d_{ae}^2 Q \tag{7}$$

where d_{ae} is the aerodynamic equivalent diameter in microns and Q is the flowrate usually taken with units of cm^3/s. Studies from Kelly et al. (2004) and Eck et al. (2000) show high deposition efficiencies (> 95%) for inertial parameter values greater than 3×10^4 $\mu m^2 cm^3/s$

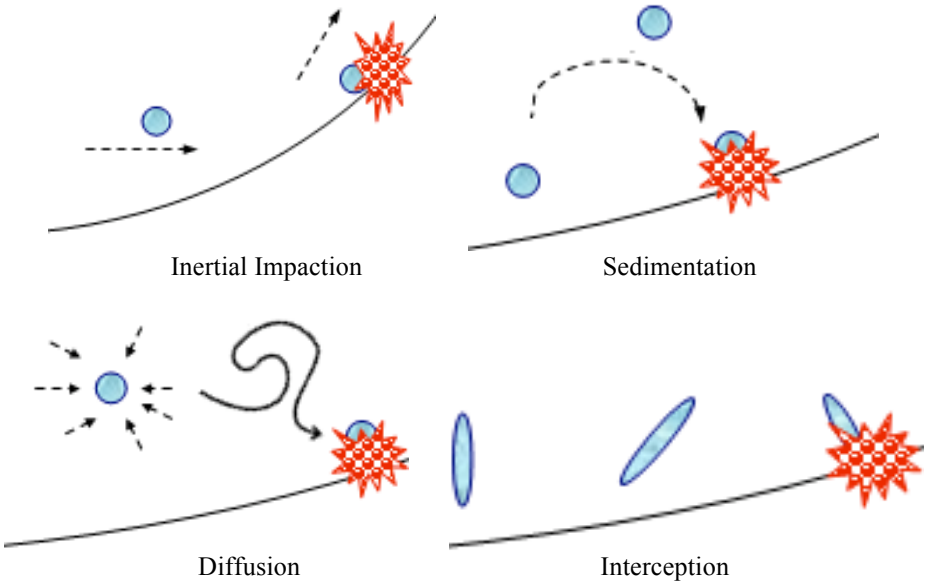

Figure 2. Particle deposition mechanisms.

The inhalation of toxic particles such as asbestos fibres and pollen through the nasal airway has been found to cause adverse health responses to the respiratory system. The physiological function of the nose is to filter the air however some particles will deposit within the nasal airway and even worse can travel through the airway down towards the lungs. While the inhalation of pollutants and toxic aerosols are undesirable, pharmaceutical aerosols are purposely introduced into the nasal cavity for therapeutic and remedial purposes. Most drug particles are usually assumed spherical with unit density as they are water based. Lighter porous drug particles have been developed for pulmonary delivery (Edwards et al. 1997), where the drug particle sizes are in the low micron to sub-micron range and deposition is targeted at the pulmonary airways such as bifurcation and the lungs. The advances in nanotechnology have provided further possibilities in delivery of drug particles in nano-size through the nasal cavity. One possible application of nanotechnology is the delivery of medicine particles in nano-size in human respiratory system. On the other hand, the adverse health effects that may follow with widespread use have some uncertainty. In the following sections, each particle type will be discussed in terms of their numerical considerations for the particle morphology.

NUMERICAL CONSIDERATIONS FOR SPHERICAL AND NANOPARTICLES

Trajectories of individual particles can be calculated by integrating the force balance equations on the particle:

$$\frac{du_i^p}{dt} = F_D\left(u_i^g - u_i^p\right) + \frac{\rho_p - \rho_g}{\rho_p} g_i + + L_i + n_i(t) \tag{8}$$

where u_i^p presents the particle velocity, ρ_p is the particle density, L_i is the Saffman lift force and $n_i(t)$ is the Brownian excitation. Aerosols (including fibres and pollen) are typically far denser than air, causing terms that depend on the density ratio, such as the pressure force, buoyancy force, virtual mass effect and Basset force to be negligibly small. $F_D\left(u_g - u_p\right)$ in Equation 8 is the drag force per unit particle mass and F_D is given by:

$$F_D = \frac{18\mu_g}{\rho_p d_p^2 C_c}\frac{C_D\, Re_p}{24} \tag{9}$$

where d_p is the particle volume equivalent diameter. Re_p is the particle Reynolds number, which is defined as:

$$\mathrm{Re}_p \equiv \frac{\rho_p d_p \left|u_g - u_p\right|}{\mu_g} \tag{10}$$

and $C_c = 1 + \frac{2\lambda}{d_p}\left(1.257 + 0.4e^{-.11 d_p/2\lambda}\right)$ is the Cunningham correction factor, where λ is the gas mean free path. The Brownian force per unit of particle mass, $n_i(t)$ in Equation 8 is modeled by a Gaussian white noise random process with an spectral intensity of $S_0 = \frac{216\mu kT}{\pi^2 \rho_p d_p^5 C_c}$, where T is the absolute temperature, and *k* is the Boltzmann constant. The details of the simulation procedure for Brownian excitation is described by Li and Ahmadi (1992). Note that the Brownian force becomes negligible for particles larger than a micron. It is noted that the gravity term, '*g*' was taken as *-9.81m/s*^{2} taken in the Y-axis and hence is applicable for an upright position. The drag coefficient C_D is given by Morsi and Alexander (1972) as:

$$C_D = a_1 + \frac{a_2}{\mathrm{Re}_p} + \frac{a_3}{\mathrm{Re}_p^2} \tag{11}$$

where the *a's* are empirical constants for smooth spherical particles over several ranges of particle Reynolds number. The equivalent aerodynamic diameter, d_{ae}, is defined as,

$$d_{ae} = d_p\sqrt{\rho_p / 1000} \tag{12}$$

NUMERICAL CONSIDERATIONS FOR POLLEN AND ROUGH SURFACES

For non-spherical particles considerable development in formulating a single correlation for any shape and orientation have been performed, notably by Haider and Levenspiel (1989) which has been proven to provide a good representation for a wide range of shape factors. Their correlation defines the C_D as a function of the particle Reynolds number and a shape factor which is given as:

$$C_D = \frac{24}{\mathrm{Re}_p}\left(1 + a\,\mathrm{Re}_p^b\right) + \frac{c\,\mathrm{Re}_p}{d + \mathrm{Re}_p} \tag{13}$$

where

$$a = \exp\left(2.3288 + 6.4581\varphi + 2.4486\varphi^2\right)$$
$$b = 0.0964 + 0.5565\varphi$$
$$c = \exp\left(4.905 - 13.8944\varphi + 18.4222\varphi^2 - 10.2599\varphi^3\right)$$
$$d = \exp\left(1.4681 + 12.2584\varphi - 20.7322\varphi^2 + 15.8855\varphi^3\right)$$

and the shape factor ϕ is defined as:

$$\varphi = \frac{A_s}{A_p} \tag{14}$$

where A_s is the surface area of a sphere having the same volume as the particle, and A_p is the actual surface area of the particle.

NUMERICAL CONSIDERATIONS FOR FIBRES

It has been reported that the accuracy of the Haider-Levenspiel method (13) decreases as the shape factor decreases (Gabitto and Tsouris 2007). A different and novel approach is by Tran-Cong et al. (2004) which defines the fibre by spherical aggregate particles clustered into a cylindrical bar configuration. This correlation will be referred to as the TC-model while the method given in Equation 13 is referred to as HL-model. Two equivalent diameters and a shape factor called the 'degree of circularity' are used for the drag correlation (Wadell 1933). The volume equivalent sphere diameter, also known as the nominal diameter, is defined as

$$d_n = \sqrt[3]{6V/\pi} \tag{15}$$

where V is the particle volume. The surface equivalent sphere diameter is defined as

$$d_A = \sqrt{4A_p/\pi} \tag{16}$$

where A_p is the projected area of the sphere. The shape factor used is based on the surface sphericity and is defined as

$$c = \pi\left(d_A/P_p\right) \tag{17}$$

where P_p is the projected perimeter of the particle in its direction of motion. The empirically defined correlation for the drag coefficient is given as:

$$C_D = \frac{24}{\mathrm{Re}}\frac{d_A}{d_n}\left[1 + \frac{0.15}{\sqrt{c}}\left(\frac{d_A}{d_n}\mathrm{Re}\right)^{0.687}\right] + \frac{0.42\left(\frac{d_A}{d_n}\right)^2}{\sqrt{c}\left[1 + 42500\left(\frac{d_A}{d_n}\mathrm{Re}\right)^{-1.16}\right]} \tag{18}$$

It should be pointed out that more details analysis of fibres transport and deposition requires tracking their translational as well as rotational motion. Simulation results for deposition in duct flows was reported by Fan and Ahmadi (1995), Kvasnak and Ahmadi (1995) and Zhang et al. 2001).

The drag correlations were implemented into FLUENT via the User-Defined Function allowing a customised drag correlation. In summary the morphological characteristics, typical mean values and numerical models to account for the different particle types are shown in Table 1.

Table 1. Summary of fibre their morphological characteristics, typical mean values and numerical models.

Porous drug particles

Shape	Typical size range	Density	Model
Sphere	10-100µm *Cheng et al. (2001)* *Suman et al. (2002)*	Low = 100, 200 kg/m^3 Normal = 1000 kg/m^3	 *Morsi and Alexander(1972)*

Ragweed Pollen

Shape	Typical size range	Density	Real Image	Modelled Image
Sphere with rough surface	16-30 µm *Crowder et al. (2002)*	550 kg/m^3 *Crawford (1949)* 840–1320 kg/m^3 *Harrington and Metzger (1963)*	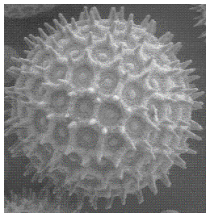 *Photo Courtesy of Dartmouth College Rippel Electron Microscope Facility*	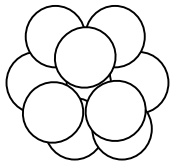 *Agglomerates of spheres method by Tran-Cong et al. (2004)*

Table 1. *continued*

Fibre

Shape	Typical size range	Density	Real Image	Modelled Image
Elongated cylinders	Asbestos Diameter (FD) < 3 μm	Asbestos 260-400 kg/m^3	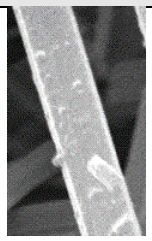 *Photograph Courtesy of the U.S. Geological Survey*	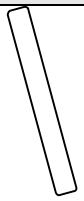 *Elongated cylinder method by Haider and Levenspiel (1989)*
	Carbon Diameter (FD) ≈ 2-15 μm	Carbon 1830kg/m^3 *Su and Cheng (2005)*		
	Fibre Length > 5 μm Aspect Ratio > 3			

RESULTS

Airflow structures

A lot of literature has covered air flow patterns within the nasal cavity, Zwartz and Guilmette (2001), Wen et al. (2008) and Horschler et al. (2003), to name a few, thus a only a brief discussion is given here while path streamlines are plotted in Figure 3. The flow increases at the nasal valve where the cross-sectional area is smallest and reaches a maximum. Entering the atrium, the velocity decreases as the nasal cavity opens up. The flow remains along the middle and lower regions of the nasal cavity and close to the septum walls rather than diverging out towards the outer meatus. A region of recirculation appears in the expanding region of the cavity near the top (olfactory region). At the nasal pharynx the velocity increases once more where a decrease in area exists.

Two cross-sectional areas located proximal to the anterior nasal valve at 2.6cm and 3.2cm were chosen to reflect the rapid changes in the flow field. A contour plot of the axial velocity (x-component of velocity) is combined with streamlines of secondary flow (y-z component of velocity). The red contours suggest the main flow field, since the horizontal direction of flow is in the x-axis. By applying directional streamlines, secondary flow features such as vortices can be visualised. The air enters the nostril inlets with a vertical direction. As the distance increases from the anterior tip of the nostrils, the nasal geometry becomes thinner and narrow as the airstream turns posteriorly, approximately 90^o towards the nasopharynx. This transition coupled with the narrowing geometry forces a majority of the flow to emerge from the outer walls from the septum and directed inwards. The presence of the wall along with the bulk flow that exists in the upper regions restricts the flow in the lower regions (light blue color) and forces the flow to recirculate thus formulating vortices (Figure 4 and Figure 5).

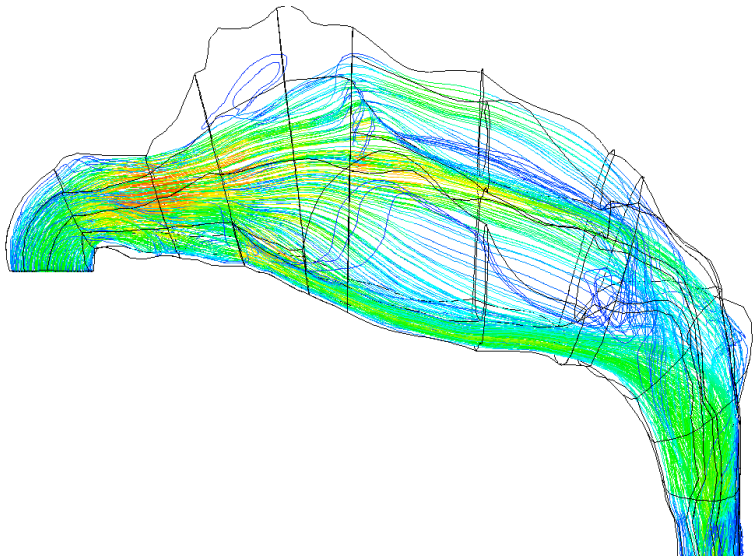

Figure 3. Path streamlines coloured by velocity magnitude. A region of recirculation is found near the roof of the nasal cavity. The normalised distance spans from the average center of the two nostril openings in the x-axis, to the nasopharynx where the two cavities have joined completely.

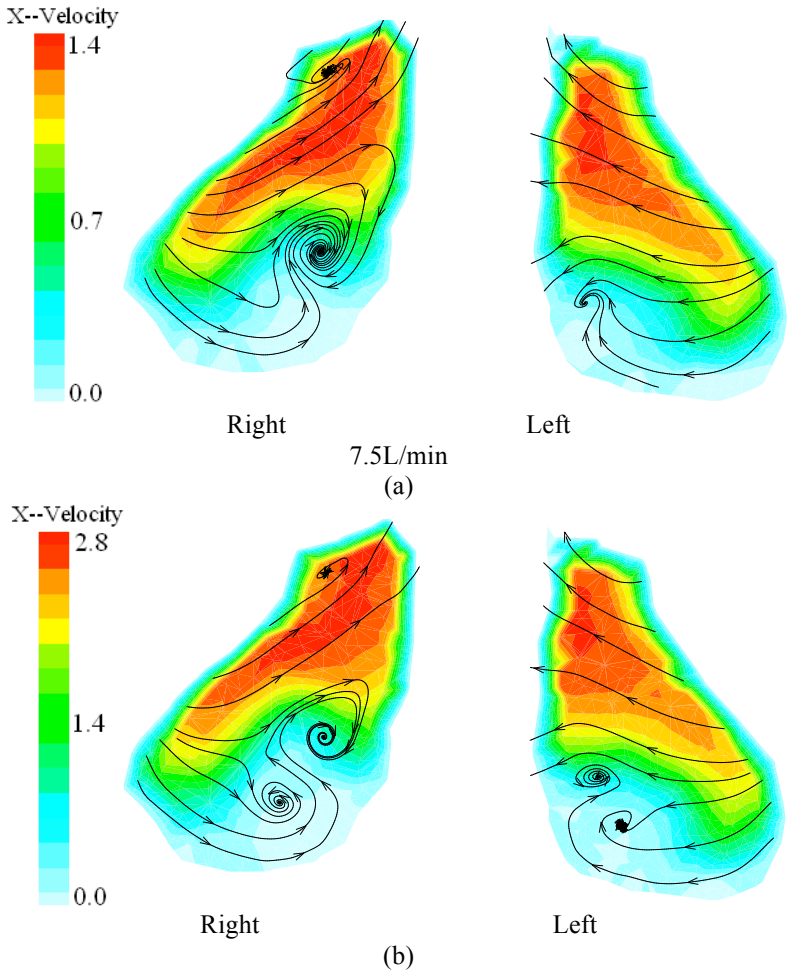

Figure 4. Velocity field in the coronal cross-section located at 2.60 cm from the anterior tip of the nose, (a), at flow rate of 7.5L/min, (b) at flow rate of 15L/min.

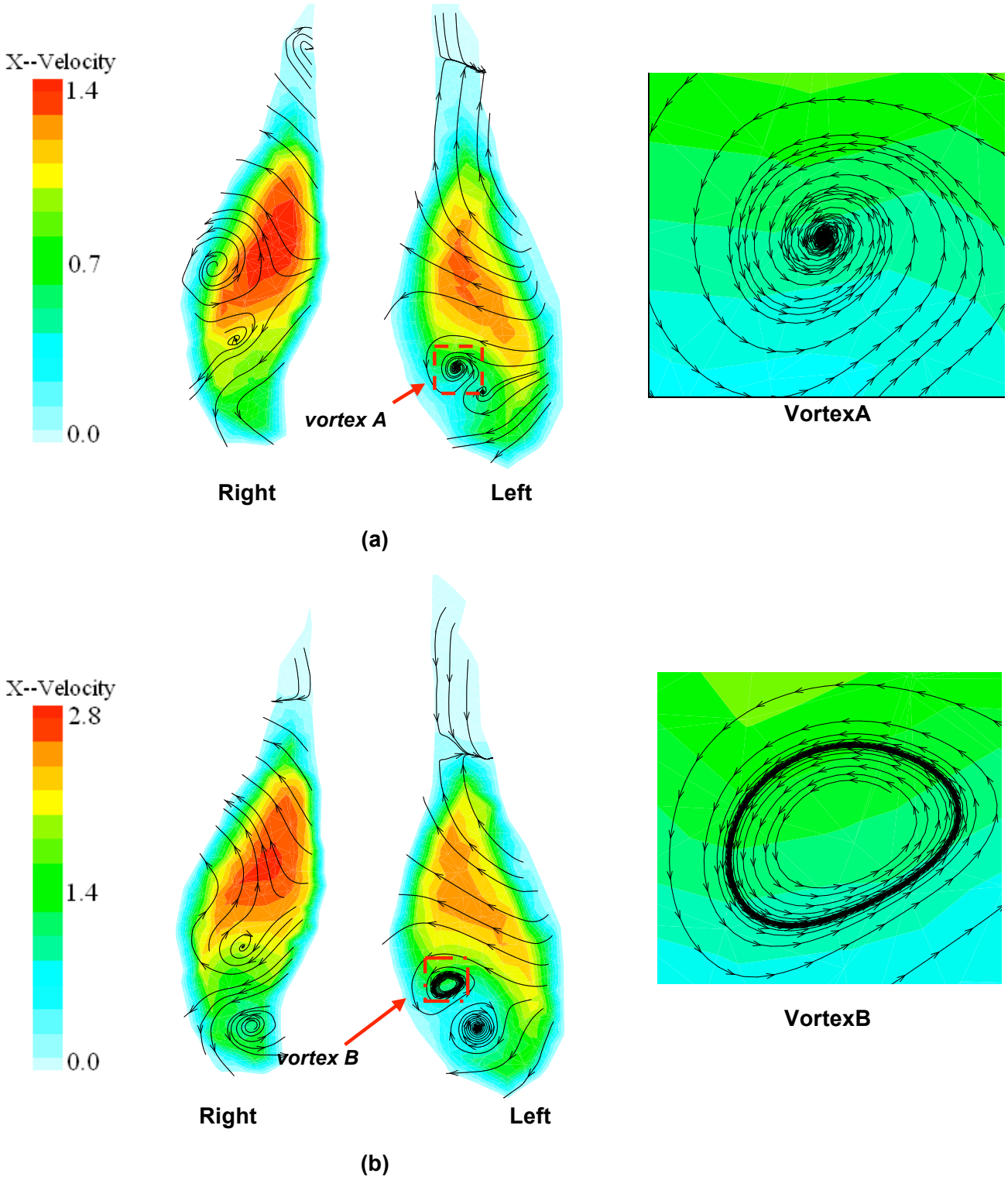

Figure 5. Velocity field in the coronal cross-section located at 3.20 cm from the anterior tip of the nose, (a), at flow rate of 7.5L/min, (b) at flow rate of 15L/min.

The cross-section located at 2.6cm from the anterior tip of the nose shows two vortices in the right cavity and one in the left for a flow rate of 7.5L/min (Figure 5a). The cross-section located at 3.2cm from the anterior tip of the nose shows the bulk flow concentrated more centrally as the air stream develops (Figure 7). At a flow rate of 7.5L/min, there are two vortices in the left cavity

while in the right cavity some recirculation occurs forming weaker vortices (Figure 5a). The direction of the streamlines in vortex A all point to the centre of the vortex, which demonstrates that the axial velocity gradient is positive and the pressure gradient is negative along the axial direction (Escudier 1988; Stabl 1992).

In further studies by the author in Zamankhan et al (2006) performed a series of computer simulation for air flows through the nose under laminar flow condition. Their simulation results were used to fit an algebraic expression for variation of the friction factor in the nose passage with Reynolds number. Accordingly,

$$f = \frac{47.78}{\mathrm{Re}}\left(1 + 0.127\,\mathrm{Re}^{0.489}\right) \tag{19}$$

Here the friction coefficient is defined as $f = \dfrac{\Delta p / \rho}{L u_m^2 / 2d}$, with flow Reynolds number, given as $Re = \dfrac{\rho_g u_m d}{\mu}$, where $\Delta \mathrm{p}$ is the average pressure drop between the nostril and nasopharynx, L is the passage length, d is the average hydrodynamic diameter of the coronal sections and $\mathrm{u_m}$ is the average flow velocity at the nostril.

DEPOSITION PATTERNS OF POROUS DRUG PARTICLES

Monodispersed particles in the range of 1-30μm were released passively into the nasal cavity with flow rates of 5, 7.5, 10 and 15L/min. The deposition of particles over a range of the inertial parameter is shown in Figure 6 in comparison with experimental results. The results from Kelly et al. (2004) were empirically defined by the equation associated with the data which is given as:

$$\eta = 1 - \exp\left(-\left(\alpha \cdot d_{ae}^2 Q\right)^{\beta}\right) \tag{20}$$

where the coefficients are, α = 5.86e-5, β = 2.1892.

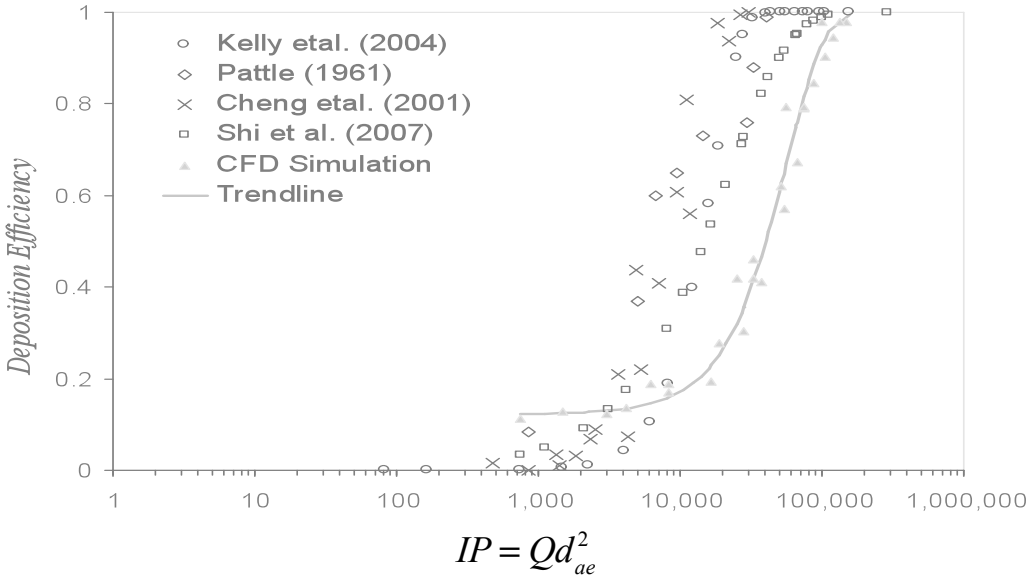

Figure 6. CFD simulation results for total deposition of particles against Inertial Parameter compared with the experimental data.

The differences in deposition may be attributed to the inter-subject variability between the nasal

cavity models obtained by Kelly et al. (2004) (53 year-old non-smoking Caucasian male), with the model used in the present study (25 year-old Asian male) while Häußerman (2001) also states that nasal cavity replicate casts with wider airways can cause less deposition due to secondary flow. Furthermore, Kelly et al. (2004) points out, that differences in comparison of particle inertial deposition with different nasal cavity models can be explained by inertial impaction considerations. For $d_{ae}^2 Q$ values less than 2000 μm^{2}cm^3/s particles have a short relaxation time, which allows the particles to adjust to flow streamlines and hence the effect of different geometries is less significant. Accordingly the comparison between the deposition curve of the CFD simulation and the experimental data is fairly similar. As the value of $d_{ae}^2 Q$ increases the particles relaxation time increases and the particles are more likely to continue a linear trajectory that deviates from a curving streamline. The differences in geometries that cause curvatures in streamlines are therefore significant for larger inertial particles.

It is known that current nasal delivery devices produce particle distribution sizes with a mean of 50μm. Particles in this size range exist in the inertial regime where deposition by impaction is relevant. The idea of low-density porous drug particles lightens the particle inertial properties however the particle inertia is more sensitive to the particle size rather than the density. The inertial parameter, *IP* incorporates both the volume equivalent spherical diameter along with the particle density which is equivalent to the particle aerodynamic diameter. Thus large porous drug particles will have an equivalent water-based particle with a diameter that is smaller while exhibiting the same aerodynamic features. Deposition efficiencies may be obtained by numerical simulation or by taking advantage of the inertial parameter. In this case, interpolation of the *IP* for 50μm particles at different densities according to the empirical correlations of Equation 20 is given in Table 2. The particle deposition patterns in the nasal cavity show a high concentration of deposition of particles in the frontal area for all three densities (Figure 7). For densities of 100 and 200 kg/m^3 a portion of the particles is seen to deposit onto the upper half of the septum walls of both sides of the cavity. This suggests that the fluid flow is significant close to the inner septum walls forcing the particles into this region. A second concentration of deposited particles occurs at the back of the nasal cavity where the flow changes directions from horizontal to vertically downwards. The change in the flow direction isn't accomplished by the particles which lead to impaction of the particles at this region. For a density of 1000 kg/m^3 most particles are deposited in the frontal area with only a small proportion of particles getting through the nasal valve region where the particles finally impact onto the upper half of the septum wall in the right nasal cavity.

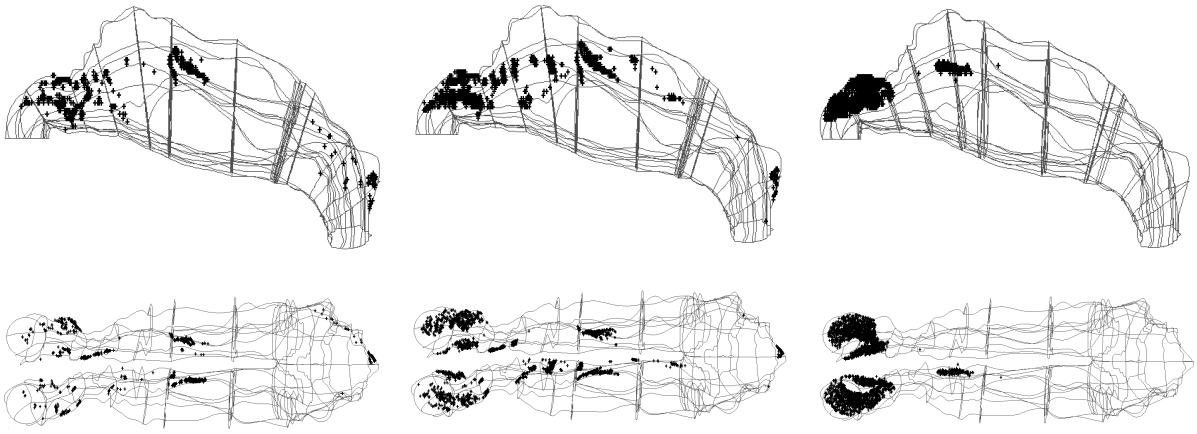

50μm 100 kg/m^3 **50μm 200 kg/m^3** **50μm 1000 kg/m^3**

Figure 7. Local deposition patterns for ultralarge drug particles that exhibit different densities.

Safe and effective therapeutic drug delivery through the nasal cavity is dependent on the targeted delivery regions. The nasal cavity can be sub-divided into three main functional regions;

the nasal vestibule, the respiratory region and the olfactory region. Where the vestibule purifies and filters the air and the olfactory region allows the sense of smell, the respiratory region has a mucosa zone that traps particles while the sub-mucosa zone is directly linked to the systemic circulation. This region is considered to be the major site for drug absorption into the systemic circulation as it exhibits high absorptive capacity (Shipper et al. 1991). By formulating different density drug particles, different deposition sites can be achieved. The differences found are particularly attributed to lowering the density of a particle will lower the particle's inertial parameter. This suggests that the particle has the ability to negotiate sudden changes in the flow field thus its particle relaxation time is reduced (*i.e.* the amount of time required to adjust to the flow field change). Therefore the potential of developing lower density particles for therapeutic delivery can provide different deposition sites which may lead to more efficient targeted delivery of drugs.

NANO-PARTICLE DEPOSITION

The results of nano-particle transport and deposition in the nasal passages as reported by Zamankhan et al. (2006) are summarised in this section. The study was performed for the breath rate of 4 to 12 l/min in one nasal passage. The influence of Brownian motion was included in these analyses. Figure 8 shows the capture efficiencies of the nasal passage for 1 to 30 nm particles for different breathing rates. This figure shows that the capture efficiency decreases with increasing particle size. The capture efficiency also decreases as the breathing rate increases. These observations suggest that for particles smaller than 30 nm, the deposition is mainly controlled by diffusion process.

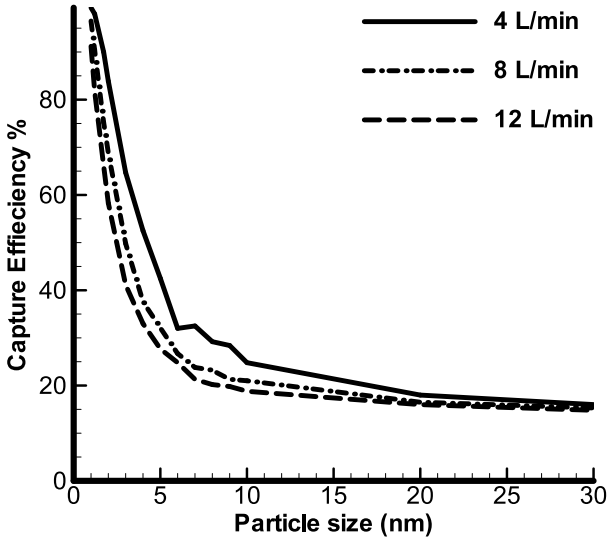

Figure 8. Simulated nasal passage capture efficiencies for different particle sizes and different breathing rates.

For breathing rates of 10 L/min, Figure 9. compares the simulation results with the available experimental data reported by a number of authors for nasal passages. While there are some scatters in the experimental data, this figure shows that the predicted capture efficiency is in good agreement with the experimental data, particularly, for particles smaller than 20 nm. Additional details and deposition rate for other breathing rate were reported by Zamankhan et al (2006).

Since the deposition of nano-particles is dominated by the diffusion process, it is expected that the Peclet number may be used as the relevant nondimensional parameter. For the nose, the effective Peclet number may be defined as,

$$Pe = \frac{Q}{DL_s}, \tag{21}$$

Here, Q is the flow rate through the nose and L_s is a characteristic length scale.

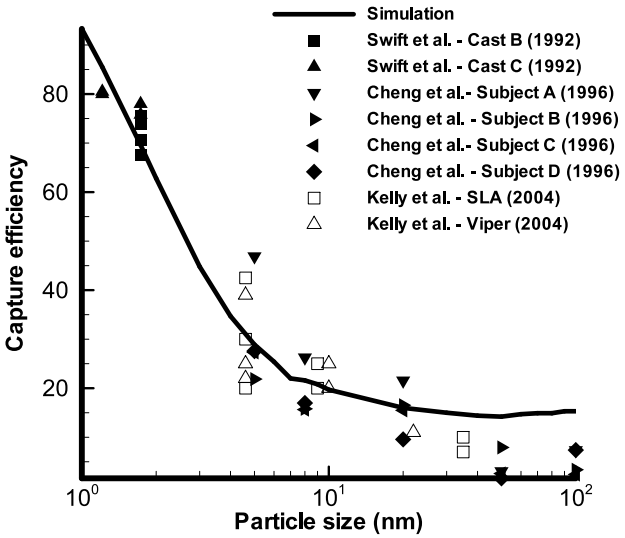

Figure 9. Comparison of the simulation and experimental data for nasal capture efficiency for nano-particles under different breathing rate of 10 L/min.

Figure 10 shows the predicted capture efficiency versus Peclet number. For L_s the length of the nasal passage was used. It is seen that the simulation data for a range of parameters collapse to a single curve. A fitted curve to data as suggested by Zamankhan et al. (2006) is given as

$$\eta = 100(1 - 0.88e^{-218Pe^{-0.75}}). \tag{22}$$

The fitted equation is in good agreement with the simulation results. As the Peclet number increases, that is the particle size increases, some scatters appear in the simulation data. This suggests that for larger particles, diffusion is not the only mechanism for deposition.

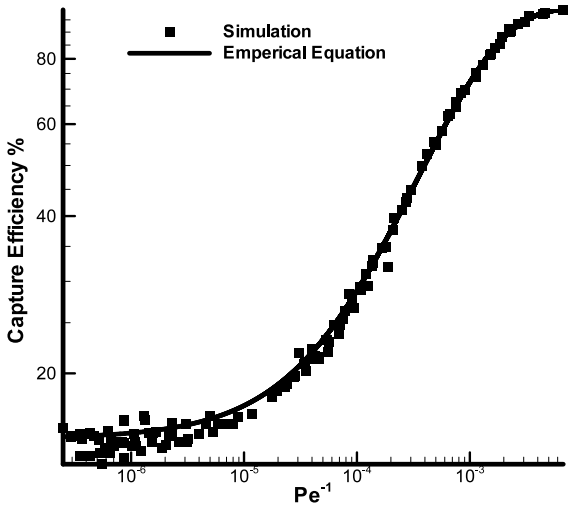

Figure 10. Variation of nasal capture efficiency with Peclet number.

DEPOSITION PATTERNS OF POLLEN AND ROUGH SURFACES

Pollen can be categorically defined as a sphere-like particle with a rough surface, especially allergenic kinds such as ragweed. The pollen may be modelled as a cluster of spheres to form a rough surface and the technique developed by Tran-Cong et al. (2004) is adopted herein. During

the pollen season, pollen in the air can either be wet or dry according to the stage of pollen development. The dry pollen lacking water content was found to have a density of 550kg/m^3 (Crawford 1949) while wet pollen with moisture has a density of 1320kg/m^3 (Harrington and Metzger 1963). In the current simulation only the dry pollen was considered as this is more justifiable in terms of the developed drifting pollen in the air. As aforementioned, the effects of a higher density lead to an increase in the inertial property thus enhancing the impactability of the particle.

Two pollen sizes 16μm and 30μm were investigated and the fate of each pollen was individually tracked. It was found that high deposition occurs in the frontal regions within the nasal vestibule (Figure 11). In between Region 2-3 lies the nasal valve region which is known to have the smallest cross-sectional area, thus causes acceleration of the fluid flow and particles. Beyond the nasal valve the particles are seen to deposit in the upper region of the nasal cavity, due to the momentum of the particles exiting the nasal valve. The deposition of particles in Region 6 may also be the cause of irritation and inflammation to the mucosal walls. Further along the nasal cavity, deposition is also seen at the back where the flow changes direction at 90^o degrees, which suggests that the particle's inertia is too high to negotiate such a sharp turn and that the nasopharaynx serves as an additional air filtration system for large particles (Figure 12).

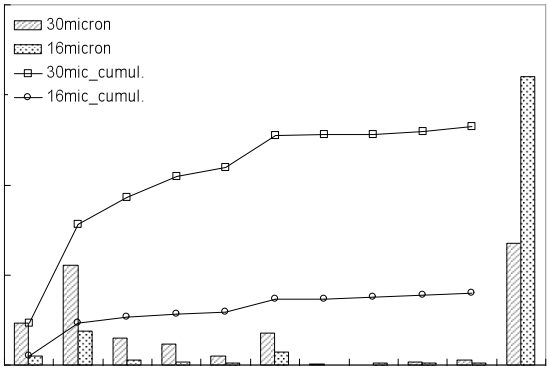

Figure 11. Cumulative deposition efficiency and regional deposition for 16μm and 30μm pollen particles.

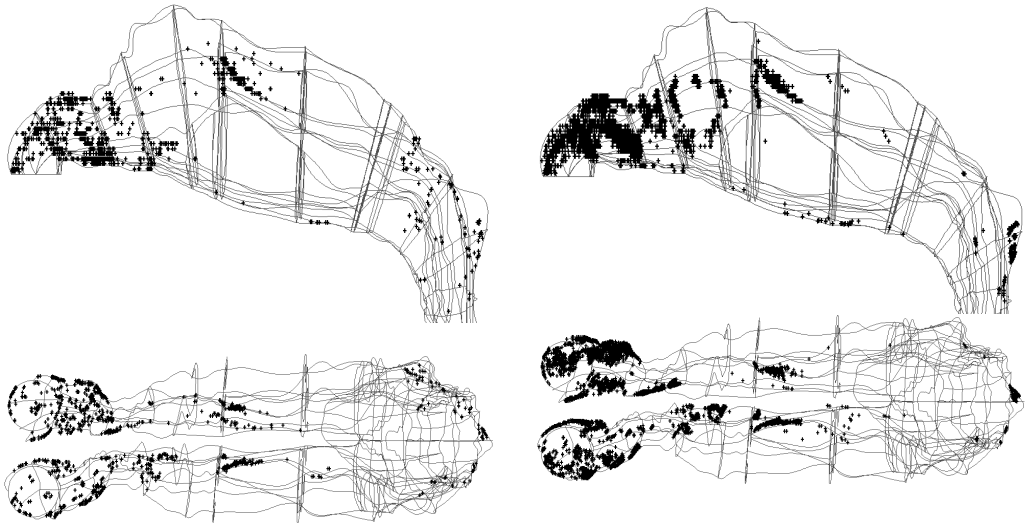

16μm, 550 kg/m^3 **30μm, 550 kg/m^3**

Figure 12. Deposition patterns for 16μm and 30μm pollen particles.

A comparison between a pollen particle with a normal spherical particle having the same inertial parameter but different drag correlation is given in Table 3. The effects of the increased drag coefficient pertaining to the Tran-Cong et al. (2004) correlation produces a higher deposition of spherical particles in comparison with near-spherical particles. Near the entrance of the airway, the drag coefficient is low for both particles and steadily increases and reaches large values near the nasopharaynx region (Figure 13).

Table 3. A comparison of particle deposition efficiency for 16μm and 30μm pollen particles against an aerodynamic sphere

Density	$d_{g,p}$	$d_{a,p}$	**Inertial Parameter (IP)**	**Deposition** *%sphere*	**Deposition** *%pollen*
550	16	11.86	23,443	30.3%	19.9%
550	30	22.25	82,500	86.0%	66.2%

This is found through the particle Reynolds number which is dependent on the slip velocity between the particle and the fluid velocity (Figure 14). The increased drag coefficient assists in slowing down the particle's momentum and thus reducing the particle relaxation time (i.e Stokes number) required by the sudden changes in the flow field. The slip velocity is reduced and significant effects occur after the normalised x-position of x=0.55, around the middle region. This reduction in the slip velocity in turn reduces the particle Reynolds number, thus increasing the drag coefficient where a very small amount of deposition results in this later region.

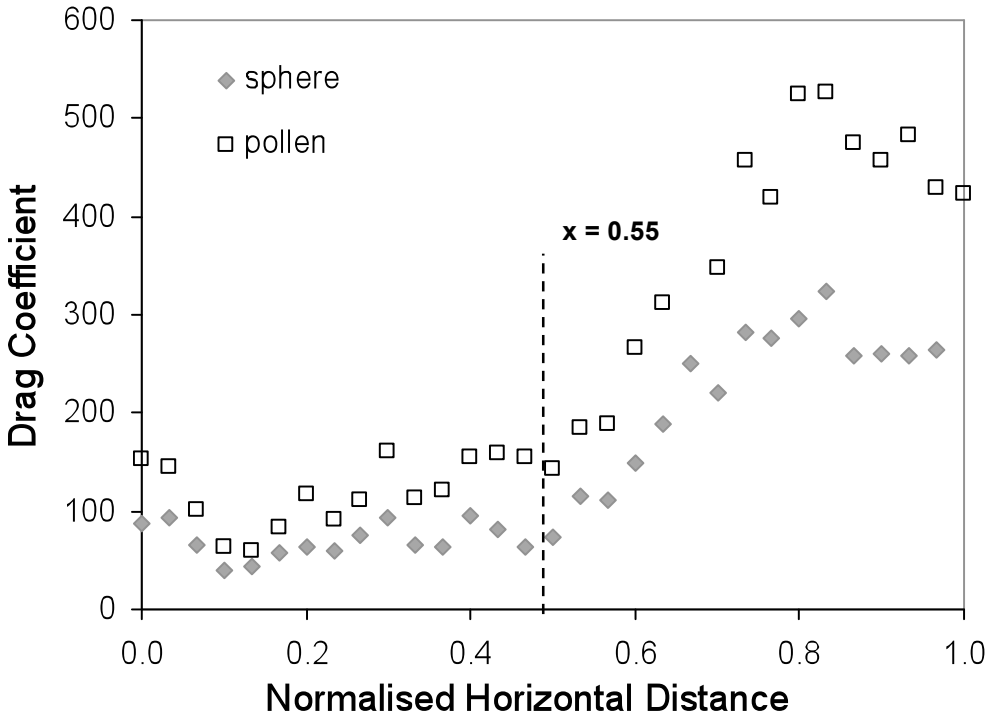

Figure 13. A comparison of the variation of the local average drag coefficient variation along the horizontal axial distance for a 30μm pollen particle and an aerodynamic equivalent sphere. (Compare with Figure 14).

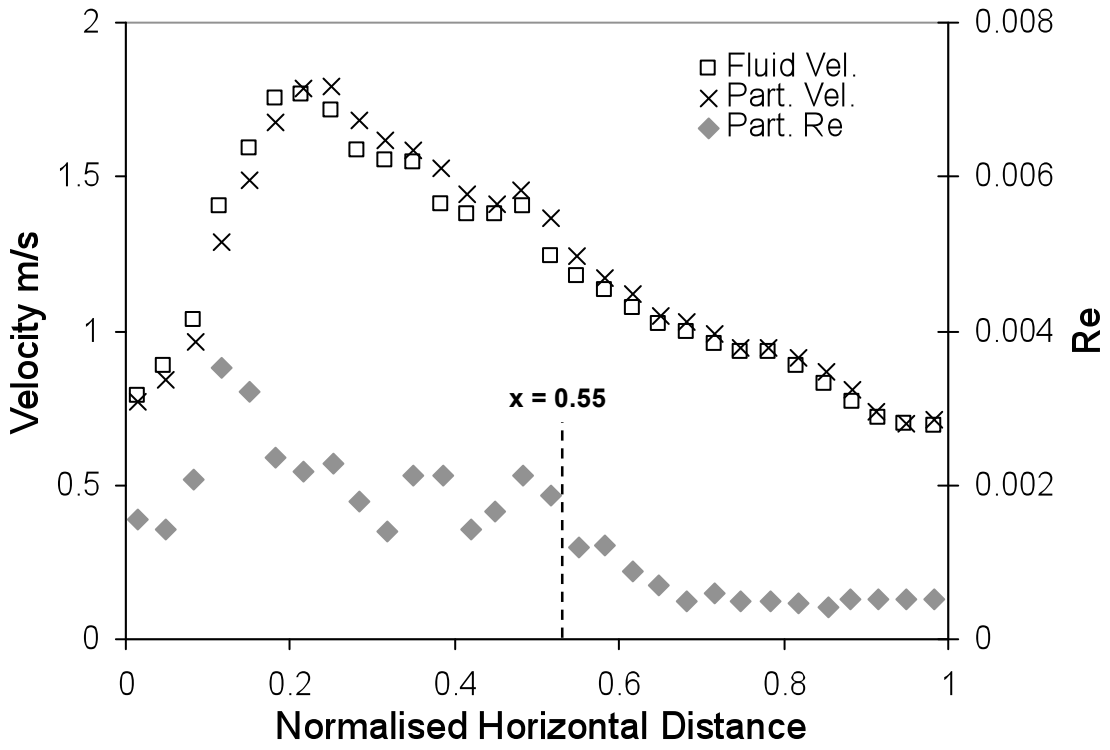

Figure 14. Fluid and particle velocity profile variation along the horizontal axial distance for a 30μm pollen particle. The particle Re number variation is also plotted which is a function of the velocity difference between the fluid and particle.

DEPOSITION OF ASBESTOS FIBRE

Typical values for carbon and asbestos fibres found in literature are summarised in Table 6.1. The toxicity of the fibres has been linked to its length where fibre deposition in the lungs can be carcinogenic. The CFD simulated deposition values shown in Figure 15 is the average deposition from the left and right cavities. The effects of fibre length on the two fibre types are markedly different. Deposition of asbestos fibres in the nasal airway is low and exhibits little variation despite the significant variation in length. The low deposition rates (14%) suggest that inhalation of the asbestos fibres will lead to deep respiratory deposition such as the lungs. In contrast the carbon fibres increase from 18% to 80% in deposition as the fibre length increases from 10 to 300 μm. The cross-sectional diameter for the carbon fibres is approximately three times that of asbestos while the density is six times as great. The length for carbon therefore becomes more significant due to a greater mass per unit length.

Table 4. A comparison of particle deposition efficiency for Asbestos, Carbon fibre and other arbitrary fibres with varying ρA_{cross} values.

	Density *(kg/m^3)*	*Diameter* *(μm)*	ρA_{cross} *(kg/m)*	*Length* *(μm)*	d_{ae} *(μm)*	*Equivalent* d_{ae} *total deposition (%)*
				10	1.09	**0.00**
Asbestos	300	1	300	100	1.44	**0.01**
				300	1.59	**0.02**
				10	7.60	**10.1**
Carbon fibre	1830	3.66	19390	100	11.38	**42.8**
				300	12.84	**60.1**
				10	5.49	**2.8**
Fibre 1	1000	3.56	10000	100	8.20	**13.5**
				300	9.25	**21.2**
				10	10.69	**35.1**
Fibre 2	3190	4	40000	100	16.18	**90.7**
				300	18.31	**98.1**

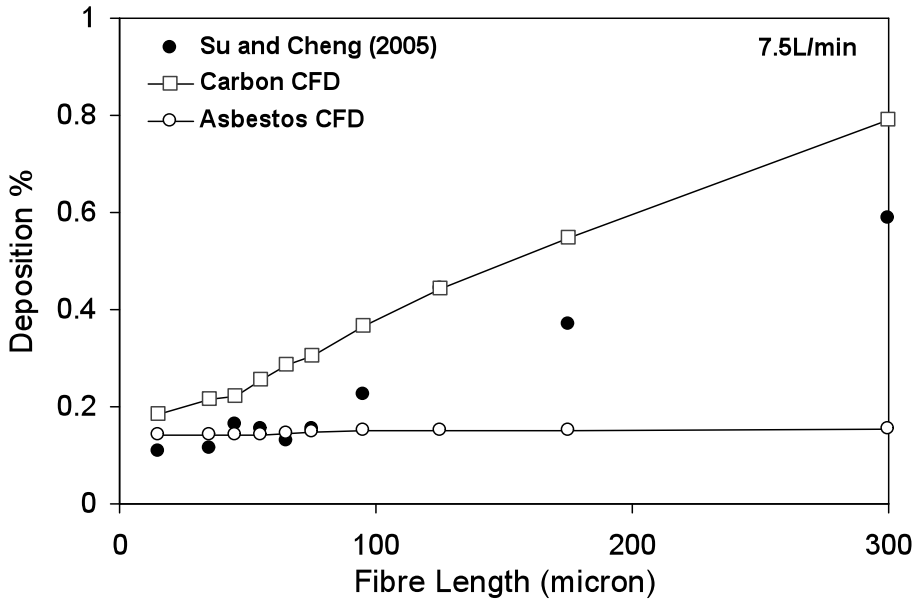

Figure 15. Total deposition efficiency for asbestos and carbon fibres at different fibre lengths.

The deposition patterns produced for the two different fibres show very sparse deposition for asbestos (Figure 16). The main deposition regions for both fibre types are found in the middle airway at the inner septum walls and also at the back region at the nasopharaynx region. High deposition is also found near the nasal valve region where flow acceleration and deceleration occurs. Due to the Lagrangian tracking methodology the deposition sites shown consider only particle deposition by inertial impaction, where it was found by Su and Cheng (2005) that fibre deposition in the nasal airway is mainly due to impaction and that short fibres could have the same deposition fraction as long fibres in a specific nasal airway region or subregion, as long as the inertial parameter for both fibres are in the same range. However for asbestos ($d_{ae} \approx$ 1μm) at low flow rates such as 7.5 L/min the inertial parameter is low and deposition by interception may have a slight increase for very long fibre lengths. Deposition by interception can occur if the particle travels close enough to a surface of the airway passages where an edge of the particle touches the surface. Usually the fibre length determines whether the particle will be intercepted. Typical fibres with a diameter of 1μm and a length of 200 μm have been found to deposit in the bronchial tree (Sussman et al. 1991). Although the nasal airway is more treacherous in comparison to the tracheobronchial airway, the nose is much larger in size and the effects of deposition of long fibre lengths would be marginal.

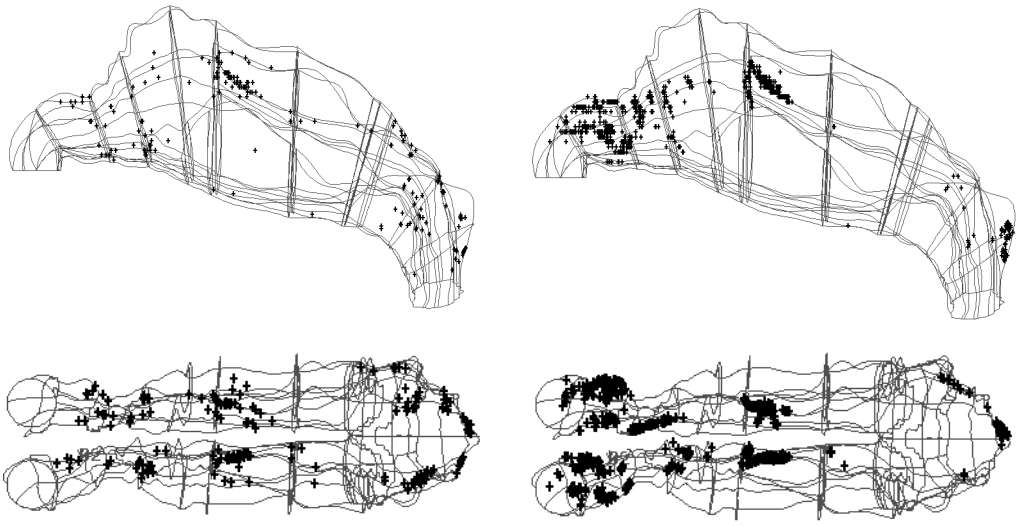

Asbestos Fibre, length = 100μm **Carbon length = 100μm**

Figure 16. Deposition patterns for asbestos fibres and carbon fibres at a fibre length of 100μm at a flow rate of 7.5L/min.

COMPARISON OF FIBRE AND SPHERICAL PARTICLE DEPOSITION

Normalisation of the fibres can be performed through correlations from (Stöber 1972) for an equivalent aerodynamic diameter (d_{ae}) given as:

$$d_{ae} = d_{ve}\sqrt{\rho \big/ (1000 \cdot \kappa)} \tag{23}$$

where d_{ve} is the volume equivalent diameter, ρ is the density of the fibre and κ is the dynamic shape factor for a prolate spheroid. The dynamic shape factor taking the length oriented perpendicular to the flow is given as:

$$\kappa_{\perp} = \frac{\frac{8}{3}\left(\beta^2 - 1\right)\beta^{1/3}}{2\beta^2 - 3 \big/ \sqrt{\beta^2 - 1}\, ln\left(\beta + \sqrt{\beta^2 - 1}\right) + \beta} \tag{24}$$

and also for the length oriented parallel to the flow is given as:

$$\kappa_{||} = \frac{\frac{4}{3}\left(\beta^2-1\right)\beta^{1/3}}{2\beta^2-1/\sqrt{\beta^2-1}\,ln\left(\beta+\sqrt{\beta^2-1}\right)-\beta} \tag{25}$$

where β is the aspect ratio and is defined as the ratio of the fibre length to the diameter. For random orientation of the fibre, the shape factor is a combination of the two orientations and is given as:

$$\frac{1}{\kappa_R} = \frac{1}{3\kappa_{||}} + \frac{2}{3\kappa_{\perp}} \tag{26}$$

Taking the random orientation for the dynamic shape factor, the equivalent aerodynamic diameter range for carbon fibre is 7.6-12.8 μm for lengths of 10-300 μm respectively. For asbestos fibres at the same length range, the d_{ae} range is 1.0-1.6 μm. This is due to the properties of asbestos exhibiting a light density and small cross-sectional diameter causing the dae to be independent of its length.

The deposition of the carbon and asbestos fibres over a range of the inertial parameter is used to compare against previous studies of total deposition efficiencies of monodispersed spherical particles over the nasal cavity as an entire unit (Figure 17). The deposition efficiency increases as the inertial parameter increases. The range in which the deposition efficiency reaches 90% or more is from 20,000 (Cheng et al. 2001) to 50,000 (Su and Cheng 2005). The simulation results used the TC-model and show the combined deposition efficiency for the left and right cavity. For $IP <$ 10,000 the deposition efficiency is higher for the simulation than for Su and Cheng (2005). The higher values for the smaller inertial particles may be improved by the addition of a wall roughness model (Shi et al. 2007).

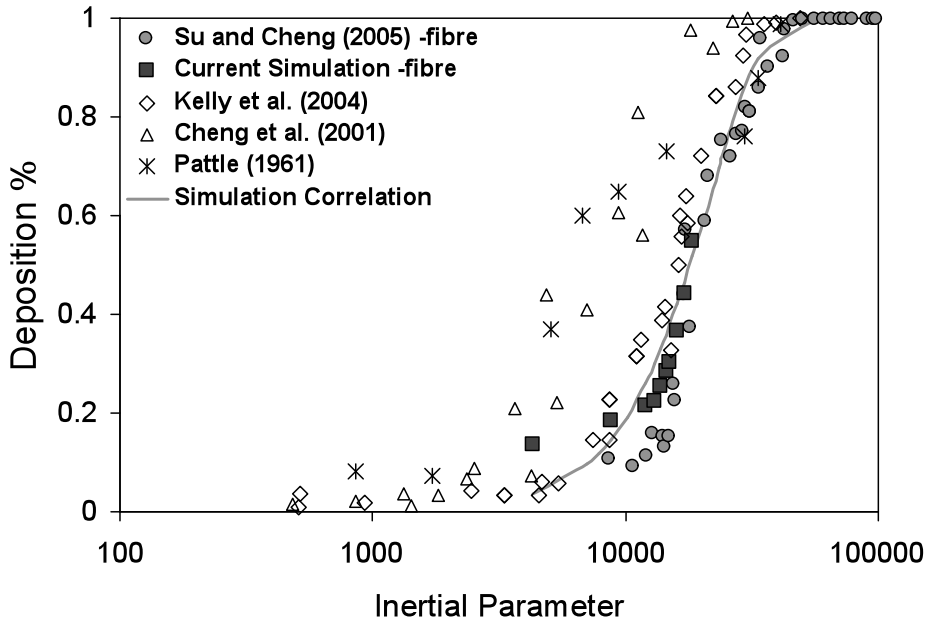

Figure 17. Comparison of deposition efficiencies between fibres and spherical particles using the Inertial Parameter.

Similar to Kelly et al. (2004) empirical correlation given in Equation 20, a correlation for the fibre deposition efficiency was found using MatlabR2006b® (Mathworks USA) software to program the Levenberg-Marquardt algorithm for constant determination. The coefficients for the

correlation given in Equation 20 are α = *4.654e-5*, β = *2.054*. The deposition efficiency curve helps to predict the deposition for a given aerodynamic diameter and flow rate. With the production of man-made fibres, there is an opportunity to control properties of the fibre that may lead to adverse health effects such as the fibre length. In the case of carbon fibres, the longer fibre lengths help increase deposition within the nasal cavity thereby reducing the potential deep lung inhalation. Conversely deposition of asbestos fibres was found to be independent of their lengths given the lighter density and smaller diameters. By taking the product of the density with the cross-sectional area, the parameter of mass per unit length, ρA_{cross} [kg/m], is used to define the resulting d_{ae}. Table 4 shows the significance of the fibre lengths on the effects of d_{ae} for different ρA_{cross} values. The deposition of the fibres can then be predicted by using the resultant d_{ae} for the fibre in question and applying the deposition efficiency curve correlation (Equation.21). The ρA_{cross} value for asbestos and carbon fibre is 300 and 19390, respectively. As ρA_{cross} increases, d_{ae} increases as expected but is most significant in the smaller length range.

CONCLUSION

The effects of particle morphology on deposition patterns and deposition efficiencies were found to be significant for nasal airway deposition. In the human nasal cavity, the dominant mechanism of deposition is by inertial impaction, especially for particles greater than 5μm at low flow rates (7.5-15L/min). Under these conditions, the inertial parameter is a useful tool that allows comparisons between particles that exist in this inertial framework. Thus aerodynamic factors pertinent to the particle morphology such as the shape factor must be accounted for through the drag coefficient. Appropriate empirical correlations were utilised to consider the aerodynamic flight of the typical inhalants.

It was found that porous drug particles provided different deposition sites in comparison with normal water-based drugs. This feature may provide an opportunity for pharmaceutical companies to investigate this type of drug for nasal delivery. Deposition and transport of ultrafine particles (1 to 100 nm) in the nasal cavity for different breathing rates were also discussed. The computational results for the nasal capture efficiency for nano-particles and various breathing rates in the laminar regime were found to correlate well with the ratio of particle diffusivity to the breathing rate especially for the particles smaller than 20 nm. Based on the simulated results, a semi-empirical equation for the capture efficiency of the nasal passage for nano-size particles was fitted in terms of Peclet number.

Allergenic ragweed pollen and toxic asbestos fibres were considered to investigate approximate deposition of these particles. It was found that about 20% of 16μm pollen particles deposited in the main airway while for 30μm pollen particles, 66.2% deposited. These values were smaller when compared with a sphere having the same aerodynamic diameter which indicates that the drag coefficient for pollen is greater than for a spherical particle. For asbestos fibres, where the density and cross-sectional diameter is small, the fibre length is seen to be insignificant for the deposition efficiency. It was seen that the deposition increased from 8.7%-9.6% for an increase in fibre length of 10μm to 300μm. Conversely, carbon MMVFs with higher density and larger cross-sectional diameter exhibits greater mass per unit length, thus its deposition increased from 14%-50% over the same fibre length range. This comparison supports the current practice of replacing asbestos with carbon MMVFs in building materials in the prevention of respiratory diseases, where deposition of the fibres in the nasal cavity is increased, reducing deep lung deposition. It is imagined that these results may assist in the design of new aerosols and guide practical clinical tests for toxicological.

FUTURE CHALLENGES

One of the parameters that affect particle trajectory is the airway geometry. In these studies only one geometry was used. A larger sample of nasal geometries is needed to determine what geometry features are dominant in affecting the gas phase which in turn will affect the particle trajectory. However obtaining CT scans, processing the images, and converting the data into a computational model is still a very time consuming practice. Additionally there has been little investigation of how much influence the movements of the nasal walls in terms of its dilation

during nasal obstruction. In every study thus far, the walls have been assumed to be rigid in numerical simulations and replicate cast experiments. The study of fluid-structure interaction is still a difficult stream as it involves both statics and dynamics equations that need to be coupled through an interface. This is especially difficult when dealing with highly complex geometries such as the nasal cavity.

REFERENCES

Chang, H.K, Flow dynamics in the respiratory tract, In Respiratory Physiology, an Analytical Approach, eds. H.K. Chang and M. Paiva. New York: Dekker, 1989.

Cheng, Y. S., Holmes, T. D., Gao, J., Guilmette, R. A., Li, S., Surakitbanharn, Y., and Rowlings, C., Characterization of nasal spray pumps and deposition pattern in a replica of the human nasal airway, *J. Aerosol Med.*, 14, 2001, 267-280.

Cheng, Y. S., Yeh, H. C., Smith, S. M., Cheng, K .H. and Swift, D. L., Deposition of ultrafine particles in the nasal and tracheo-bronchial airways, *J. Aerosol Sci.*, 29, 1998, S941-S942.

Churchill, S., Shackelford, L. L., Georgi, N. and Black, M., Morphological variation and airflow dynamics in the human nose, *Am. J. Human Bio.*, 16, 2004, 625-638.

Crawford, J. H., Determination of the specific gravity of ragweed pollen (Ambrosia elatior) and conversion of gravity sample counts to volumetric incidence, *Pub. Health Rep.*, 64, 1949, 1195-1200.

Croce, C., Fodil, R., Durand, M., Sbirlea-Apiou, G., Caillibotte, G., Papon, J. F., Blondeau, J. R,. Coste, A., Isabey, D. and Louis, B., In vitro experiments and numerical simulations of airflow in realistic nasal airway geometry, *Annals Biomed. Eng.*, 34, 2006, 997-1007.

Crowder, T. M., Rosati, J. A., Schroeter, J. D., Hickey A. J. and Martonen, T. B., Fundamental effects of particle morphology on lung delivery: Predictions of Stokes law and the particular relevance to dry powder inhaler formulation and development, *Pharma. Res.*, 19, 2002, 239-245.

Dehbi, A., A CFD model for particle dispersion in turbulent boundary layer flows, *Nuc. Eng. Des.*, 38, 2008, 707-715.

Djupesland, P.G., Sketting, A., Winderen, M. and Holand, T., Bi-directional nasal delivery of aerosols can prevent lung deposition, *J. Aerosol Med.*, 17, 2003, 249-259.

Eck, C. R., McGrath, T. F. and Perlwitz, A. G., Droplet size distributions in a solution nasal spray, *Respir. Drug Deliv.*, 7, 2000, 475-478.

Edwards, D. A., Hanes, J., Caponetti, G., Hrkach, J., Ben-Jebria, A., Eskew, M. L., Mintzes, J., Deaver, D., Lotan, N. and Langer, R., Large porous particles for pulmonary drug delivery, *Sci.*, 276, 1997, 1868-1872.

Elad, D., Liebenthal, R., Wenig, B. L. and Einav, S., Analysis of air flow patterns in the human nose, *Med. Bio. Eng. Comp.*, 31, 1993, 585-592.

Escudier, M., Vortex breakdown: Observations and explanations, *Prog. Aerospace Sci.*, 422, 1988, 189-229.

Fan, F. G. and Ahmadi, G., A sublayer model for wall deposition of ellipsoidal particles in turbulent streams, *J. Aerosol Sci.*, 26, 1995, 813-840.

Gabitto, J. and Tsouris, C., Drag coefficient and settling velocity for particles of cylindrical shape, *Powder Tech.*, 2007, 183, 2008, 314-322.

Girardin, M., Bilgen, E. and Arbour, P., Experimental study of velocity fields in a human nasal fossa by laser anemometry, *Ann. Otol. Rhinol. Laryngol*, 92, 1983, 231-236.

Gradon, L. and Podgorski, A., Experimental study on fibrous particle deposition in the human nasal cast., *J. Aerosol Sci.*, 23, 1992, 469-472.

Guilmette, R. A., Cheng, Y. S., Yeh, H. C. and Swift, D. L., Deposition of 0.005-12um monodisperse particles in a computer-milled, MRI-based nasal airway replica, *Inhal. Toxicol.*, 6, 1994, 395-399.

Hahn, I., Scherer, P. W. and Mozell, M .M., Velocity profiles measured for airflow through a large-scale model of the human nasal cavity, *J Appl. Physiol.*, 75, 1993, 2273-2287.

Haider, A. and Levenspiel, O., Drag coefficient and terminal velocity of spherical and nonspherical particles, *Powder Tech.*, 58, 1989, 63-70.

Harrington, J. B. and Metzger, K., Ragweed pollen density, *Am. J. Botany*, 50, 1963, 532-539.

Häußermann, S., Bailey, A. G., Bailey, M. R., Etherington, G. and Youngman, M. J., The influence of breathing patterns on particle deposition in a nasal replicate cast, *J. Aerosol Sci.*, 33, 2001, 923-933.

Hornung, D. E., Leopold, D. A., Youngentob, S. L., Sheehe, P. R., Gagne, G. M., Thomas, F. D. and Mozell, M. M.,

Airflow patterns in a human nasal model, *Arch. Otolaryngol Head Neck Surg.*, 113, 1987, 169-172.

Hörschler, I., Meinke, M. and Schröder, W., Numerical simulation of the flow field in a model of the nasal cavity, *Comp. Fluids*, 32, 2003, 39-45.

Inthavong, K., Tian, Z. F., Li, H. F., Tu, J. Y., Yang, W., Xue, C. L. and Li, C. G., A numerical study of spray particle deposition in a human nasal cavity, *Aerosol Sci. Tech.*, 40, 2006, 1034-1045.

Isabey, D. and Chang, H. K., Steady and unsteady pressure-flow relationships in central airways, *J. Appl. Physiol.*, 51, 1981, 1338-1348.

Itoh, H., Smaldone, G. C., Swift, D. L. and Wagner, H. N. J., Mechanisms of aerosol deposition in a nasal model, *J. Aerosol Sci.*, 16, 1985, 529–534.

Kelly, J. T., Asgharian, B., Kimbell, J. S. and Wong. B. A., Particle deposition in human nasal airway replicas manufactured by different methods. Part 1: Inertial regime particles, *Aerosol Sci. Tech.*, 38, 2004, 1063-1071.

Kelly, J. T., Prasad, A. K. and Wexler, A. S., Detailed flow patterns in the nasal cavity, *J. Appl. Physiol.*, 89, 2000, 323-337.

Keyhani, K., Scherer, P. W. and Mozell, M. M., Numerical simulation of airflow in the human nasal cavity, *J. Biomech. Eng.*, 117, 1995, 429-441.

Keyhani, K., Scherer, P. W. and Mozell, M. M., A numerical model of nasal odorant transport for the analysis of human olfaction, *J. Theo. Bio.*, 186, 1997, 279-301.

Kimbell, J., Shroeter, J. D., Asgharian, B., Wong, B. A., Segal, R. A., Dickens, C. J., Southall, J. P. and Miller, F. J., Optimisation of nasal delivery devices using computational models, *Res. Drug Del.*, 9, 2004, 233-238.

Kimbell, J. S., Segal, R. A., Asgharian, B., Wong, B. A., Schroeter, J. D., Southall, J. P., Dickens, C. J., Brace, G. and Miller, F. J., Characterization of deposition from nasal spray devices using a computational fluid dynamics model of the human nasal passages, *J. Aerosol Med.*, 20, 2007, 59-74.

Kvasnak, W. and Ahmadi, G., Fibrous particle deposition in a turbulent channel flow - An experimental study, *Aerosol Sci. Tech.*, 23, 1995, 641-652.

Li, A. and Ahmadi, G., Dispersion and deposition of spherical particles from point sources in a turbulent channel flow, *Aerosol Sci. Tech.*, 16, 1992, 209-226.

Lindemann, J., Keck, T., Wiesmiller, K., Sander, B., Brambs, H. J., Rettinger, G. and Pless, D., Nasal air temperature and airflow during respiration in numerical simulation based on multislice computed tomograpthy scan, *Am. J. Rhinol.*, 20, 2006, 219-223.

Liu, Y., Matida, E. A., Junjie, G. U. and Johnson, M. R., Numerical simulation of aerosol deposition in a 3-D human nasal cavity using RANS, RANS/EIM, and LES, *J. Aerosol Sci.*, 38, 2007, 683-700.

Macinnes, J. M. and Bracco, F. V., Stochastic particle dispersion modeling and the tracer particle limit, *Phys. Fluids A*, 4, 1992, 2809-2823.

Matida, E.A., Finlay, W. H., Lange, C. F. and Grgic, B., Improved numerical simulation for aerosol deposition in an idealized mouth-throat, *J. Aerosol Sci.*, 35, 2004, 1-19.

Morsi, S.A. and Alexander, A. J., An investigation of particle trajectories in two-phase flow systems, *J. Fluid Mech.*, 55, 1972, 193-208.

Naftali, S., Rosenfeld, M., Wolf, M. and Elad, D., The air-conditioning capacity of the human nose, *Annals Biomed. Eng.*, 33, 2005, 545-553.

Park, C. S., Müller, N. L., Worthy, S. A., Kim, J. S., Awadh, N. and Fitzgerald, M., Airway obstruction in asthmatic and healthy individuals: inspiratory and expiratory thin-section CT findings, *Radiology*, 203, 1997a, 361-367.

Park, K. I., Brucker, C. and Limberg, W. Experimental study of velocity fields in a model of human nasal cavity by DPIV, In Laser Anemometry Advances and Applications: Proceedings of the 7th International Conference, eds. Ruck, B., Leder, A. and Dopheide, D., University of Karlsruhe, Karlsruhe, Germany, 1997b.

Schreck, S., Sullivan, K. J., Ho, C. M. and Chang H. K., Correlations between flow resistance and geometry in a model of the human nose, *J. Appl. Physiol.*, 75, 1993, 1767-1775.

Schroeter, J. D., Kimbell, J. S. and Asgharian, B., Analysis of particle deposition in the turbinate and olfactory regions using a human nasal computational fluid dynamics model, *J. Aerosol Med.*, 19, 2006, 301-313.

Shi, H., Kleinstreuer, C. and Zhang, Z., Laminar airflow and nanoparticle or vapor deposition in a human nasal cavity model, *J. Biomech. Eng.*, 128, 2006, 697-706.

Shi, H., Kleinstreuer, C. and Zhang, Z., Dilute suspension flow with nanoparticle deposition in a representative nasal

airway model, *Phys. Fluids*, 20, 2008, 1-23.

Shi, H., Kleinstreuer, C. and Zhang, Z., Modeling of inertial particle transport and deposition in human nasal cavities with wall roughness, *J. Aerosol Sci.*, 38, 2007, 398-419.

Shipper, G. M., Verhoef, J. and Merkus, W. H. M., The nasal mucociliary clearance: relevance to nasal drug delivery, *Pharma. Res.*, 7, 1991, 807-814.

Stabl, W. H., Experimental investigation of the vortex flow on delta wings at high incidence, *AIAA J.*, 30, 1992, 1027-1032.

Stöber, W., Dynamic shape factors of nonspherical aerosol particles, In Assessment of airborne particles, ed. Mercer et al. Springfield, IL: Charles C. Thomas, 1972.

Su, W. C. and Cheng, Y. S., Deposition of fiber in the human nasal airway, *Aerosol Sci. Tech.*, 39, 2005, 888–901.

Subramaniam, R. P., Richardson, R. B., Morgan, K. T., Kimbell, J. S. and Guilmette, R. A., Computational fluid dynamics simulations of inspiratory airflow in the human nose and nasopharynx, *Inhal. Toxicol.*, 10, 1998, 91-120.

Sullivan, K. J. and Chang, H. K., Steady and oscillatory trans-nasal pressure-flow relationships in healthy adults, *J. Appl. Physiol.*, 71, 1991, 983-992.

Sussman, R. G., Cohen, B. S. and Lippmann, M., Asbestos fiber deposition in human tracheobronchial cast.. I. Experimental, *Inhal. Toxicol.*, 3, 1991, 145-160.

Swift, D. L., Inspiratory inertial deposition of aerosols in human nasal airway replicate casts: Implication for the proposed NCRP lung model, *Radiat. Prot. Dosim.*, 38, 1991, 29-34.

Swift, D. L. and Proctor, D. F., Access of air to the respiratory tract, In Respiratory Defense Mechanism, eds. Brain, J. D., Proctor, D. F. and Reid., L. M., Marcel Dekker, New York, 1977.

Tian, L. and Ahmadi, G., Particle deposition in turbulent duct flow- Comparison of different model predictions, *J. Aerosol Sci.*, 38, 2007, 377-397.

Tian, Z. F., Inthavong, K. and Tu, J. Y., Deposition of inhaled wood dust in the nasal cavity, *Inhal. Toxicol.*, 19, 2007, 1155-1165.

Tran-Cong, S., Gay, M. and Michaelides, E. E., Drag coefficients of irregularly shaped particles, *Powder Tech.*, 139, 2004, :21-32.

Tu, J. Y., Abu-Hijleh, B., Xue, C. and Li, C. G., CFD simulation of air/particle flow in the human nasal cavity, Proceedings of 5th International Conference on Multiphase Flow, Yokohama, Japan, 2004.

Wadell, H., Sphericity and roundness of rock particles, *J. Geol.*, 41, 2004, 310-331.

Wang, K., Denney, T. S., Morrison, E. E. and Vodyanoy, V. J., Numerical simulation of air flow in the human nasal cavity, Proceeding of the 2005 IEEE, 2005.

Wang, Y. and James, P. W., On the effect of anisotropy on the turbulent dispersion and deposition of small particles, *Int. J. of Multiphase Flows*, 25, 1999, 551-558.

Weinhold, I. and Mlynski, G., Numerical simulation of airflow in the human nose, *Eur. Arch. Otorhinolaryngol.*, 261, 2004,:452-455.

Wen, J., Inthavong, K., Tu, J. Y. and Wang, S., Numerical simulations for detailed airflow dynamics in a human nasal cavity, *Res. Physiology Neurobio.*, 161, 2008, 125-135.

Zamankhan, P., Ahmadi, G., Wang, Z., Hopke, P. H., Cheng, Y. S., Su, W. C. and Leonard, D., Airflow and deposition of nanoparticles in a human nasal cavity, *Aerosol Sci. Tech.*, 40, 2006, 463-476.

Zhang, H., Ahmadi, G., Fan, F. G. and McLaughlin, J. B., Ellipsoidal particles transport and deposition in turbulent channel flows, *Int. J. Multiphase Flows*, 27, 2001, 971-1009.

Zhang, Y., Finlay, W. H. and Matida, E. A., Particle deposition measurements and numerical simulation in a highly idealized mouth-throat, *J. Aerosol Sci.*, 35, 2004, 789-803.

Zhao, B., Zhang, Y., Li, X., Yang, X. and Huang, D. T., Comparison of indoor aerosol particle concentration and deposition in different ventilated rooms by numerical method, *Build. Env.*,39, 2004,1-8.

Zwartz, G. J. and Guilmette, R. A., Effect of flow rate on particle deposition in a replica of a human nasal airway, *Inhal. Toxicol.*, 13, 2001,109-127.